ROYAL SOCIETY
OF CHEMISTRY

PAPER

Check for updates

View Article Online
View Journal | View Issue

Disentangling the structure, optical properties, and photoluminescence emissions of NiW$_{1−x}$Mo$_x$O$_4$ (*x* = 25, 50, and 75%) solid solutions: experimental and DFT studies†

Amanda Fernandes Gouveia, [iD] *[a] Marcelo Assis, [iD] [ab] Lara Kelly Ribeiro, [iD] [ac] Eduardo de Oliveira Gomes,[a] Marcio Daldin Teodoro,[d] Elson Longo [iD] [c] and Juan Andrés [iD] *[a]

Solid solutions, formed by combining two transition metal oxides with distinct properties, offer promising potential for optimizing functional characteristics that may be lacking in the parent materials. In this study, NiWO$_4$ and NiMoO$_4$ semiconductors and homogeneous NiW$_{1−x}$Mo$_x$O$_4$ (*x* = 25, 50, and 75%) solid solutions were successfully synthesized *via* a co-precipitation method followed by heat treatment, without any surfactants or toxic solvents. Using a combination of characterization techniques—including X-ray diffraction, Raman and infrared spectroscopy, X-ray fluorescence, diffuse reflectance spectroscopy, and photoluminescence (PL) spectroscopy—alongside density functional theory calculations, we elucidate the relationship between the structure, electronic properties, and PL emissions at the atomic level. Furthermore, we propose a relay mechanism in the conduction band, where an electron transport ladder through the Ni−O−W/Mo framework acts as a driving force to modulate PL emissions.

1 Introduction

Solid solutions composed of complex metal oxides are integral to modern semiconductor technology, with applications ranging from sensor to catalysis.[1–4] This extended multifunctionality arises from the synergistic effects induced by the coexistence of multiple metal cations, partially filled d orbitals, and highly electronegative oxygen anions. Tungstates and molybdates (MWO$_4$ and MMoO$_4$, where M = Mn, Co, Ni, Zn, and Cu) hold immense potential in the field of inorganic semiconductors due to their unique physical–chemical properties.[5–12]

Among these semiconductors, nickel tungstate (NiWO$_4$, NW) and nickel molybdate (NiMoO$_4$, NM) exhibit structural stability as well as interesting electronic and electrochromic

[a] Department of Physical and Analytical Chemistry, Universitat Jaume I, Castelló 12071, Spain. E-mail: gouveiad@uji.es, andres@qfa.uji.es

[b] Department of Biosciences, Institute of Health and Society, Universidade Federal de São Paulo, Santos 11015-020, Brazil

[c] CDMF, Universidade Federal de São Carlos, São Carlos 13565-905, Brazil

[d] Physics Department, Universidade Federal de São Carlos, São Carlos 13565-905, Brazil

† Electronic supplementary information (ESI) available: Elemental analysis – XRF spectrometry, bond distances and Jahn–Teller distortion, and density of states (DOS). See DOI: https://doi.org/10.1039/d4tc05251j

properties,[13,14] which form the basis for a wide range of applications, including catalysts, photovoltaic electrochemical cells, electrocatalytic oxygen evolution reactions, and sensors, among others.[15–24] Both NW and NM are characterized by a monoclinic phase and consist of mixed-valence transition metal oxides, in which Ni^{2+} and W^{6+}/Mo^{6+} occupy octahedral sites. More specifically, NW crystallizes in the *P*2/*c* space group and *C*$_{2h}$ point group symmetry, featuring [NiO$_6$] and [WO$_6$] clusters.[7] In turn, NM belongs to the *C*2/*m* space group, also with *C*$_{2h}$ point group symmetry, but with [NiO$_6$] and [MoO$_6$] clusters.[25] This structural similarity suggests that the formation of a solid solution should be easily achievable, resulting in distinct properties compared to the pure systems. Furthermore, to the best of our knowledge, there are no reports in the literature on the successful preparation of a continuous NiW$_{1−x}$Mo$_x$O$_4$ solid solution with a monoclinic structure across the entire compositional range.

Previous experimental and theoretical investigations of solid solutions composed of tungstates[26–31] and molybdates[32,33] have provided a deep understanding of the structural and electronic property changes, helping to rationalize the design of new optical and photocatalytic materials, which are sometimes absent in the parent materials.

Specifically, Ag$_2$W$_{0.50}$Mo$_{0.50}$O$_4$[28] and α-Ag$_2$W$_{0.75}$Mo$_{0.25}$O$_4$[29] solid solutions have demonstrated that these systems exhibit

6788 | *J. Mater. Chem. C*, 2025, **13**, 6788–6798

This journal is © The Royal Society of Chemistry 2025

unique photoluminescence (PL) emissions with higher intensities than those of single-structured, α-Ag$_2$WO$_4$ and β-Ag$_2$MoO$_4$.[34] Delving deep into the evolution of the structure and electronic properties when metal cations are substituted during the formation of metal oxide solid solutions, as well as managing the relationship between the crystal structure and PL emissions, is crucial for targeted applications.[33,35] Although precise regulation of the spatial distribution of the dopant in the host lattice is an effective method to improve their properties, the experimental determination and the corresponding mechanisms involved in this process are still unclear. Theoretical investigations can greatly aid in paving the way for the rational design of novel materials with optimal composition and enhanced performance. Therefore, it is desirable and necessary to use not only characterization techniques but also advanced quantum-chemical calculation methods to further deepen the understanding of the physiochemical processes occurring during the formation of these complex solid solutions.

The considerations above led us to synthesize complex quaternary NiW$_{1-x}$Mo$_x$O$_4$ (x = 25, 50, and 75) solid solutions using a co-precipitation (CP) method, followed by heat treatment in a conventional oven, without the need for expensive surfactants or toxic solvents.

The synthesized materials were characterized using X-ray diffraction (XRD), Raman and infrared spectroscopy, X-ray fluorescence (XRF), scanning electron microscopy (SEM), ultraviolet-visible (UV-vis) diffused reflectance spectroscopy, and PL spectroscopy. These techniques were employed to evaluate the effects of W^{6+} substitution by Mo^{6+} into the NiWO$_4$ crystal structure, as well as its impact on the morphology, energy band structure, and PL emissions. Additionally, density functional theory (DFT) calculations were performed to investigate the geometry, band structure, and density of states (DOS) in detail.

The main aims of the study were twofold: (i) to investigate the local bonding patterns of [NiO$_6$], [WO$_6$], and [MoO$_6$] clusters and unveil the multicentric bonding character during the substitution process in NiW$_{1-x}$Mo$_x$O$_4$ (x = 25, 50, and 75%) solid solutions, and (ii) to model these phenomena in greater detail to gain deep insights into the structure, electronic properties, and PL emissions during the solid solution formation. These findings provide both experimental references and theoretical support for the design of these promising materials for optical applications.

2 Results and discussion

2.1 Structural analysis

The XRD patterns of the as-synthetized samples are presented in Fig. 1a. For both NW and NM, pure phases of their respective materials were obtained, and the diffractograms were analyzed based on the available crystallographic data for NW (ICSD No. 15852)[36] and NM (ICSD No. 450142).[37] Both NW and NM exhibit a monoclinic crystal structure, with NW crystallizing in the $P2/c$ space group and NM in $C2/m$. The NW structure comprises each chain of [NiO$_6$] clusters which is corner linked

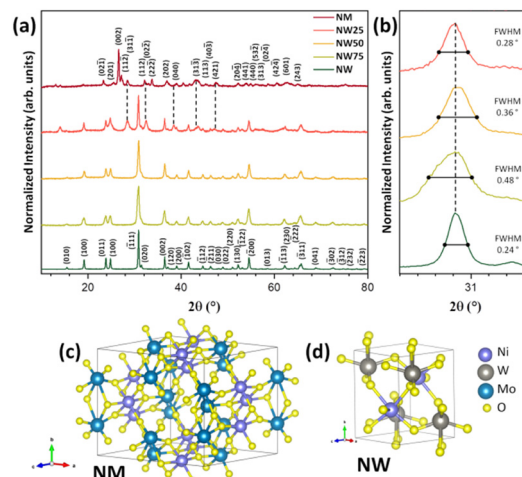Fig. 1 (a) X-ray diffraction pattern of the NW, NW75, NW50, NW25, and NM samples; (b) zoomed-in view of the ($\bar{1}$11) peak at 2θ 30.8° with full width at half maximum (FWHM) values; (c) schematic 3D representation of the NM structure with $C2/c$; and (d) schematic 3D representation of the NW structure with $P2/c$ monoclinic symmetry.

to four chains of [WO$_6$] clusters, and *vice versa*, creating open channels along the [001] direction. In NM, Ni^{2+} and Mo^{6+} cations are also coordinated with six oxygen atoms, forming [NiO$_6$] and [MoO$_6$] clusters, but these clusters are interconnected *via* edge-sharing. As a result, the three-dimensional (3D) atomic packing in both NW and NM is nearly identical, with individual [NiO$_6$], [WO$_6$], and [MoO$_6$] clusters connected to their neighboring [NiO$_6$] and [MoO$_6$/WO$_6$] clusters through edge-sharing. In other words, in both the NW and NM crystal lattices, the [NiO$_6$] and [MO$_6$] clusters are linked *via* Ni–O–M bridging links (where M = W^{6+} or Mo^{6+}).

For the NW75 and NW50 samples, only peaks corresponding to the NW phase were detected by XRD. However, in the NW25 sample, some peaks corresponding to the NM phase were also detected, including (11$\bar{2}$), (112), (040), (31$\bar{3}$), and (421).

Moreover, local stress and strain are generated due to the unit cell volume difference between the $P2/c$ and $C2/m$ phases. In Fig. 1b, changes in full width at half maximum (FWHM) values in the range of 10 to 80° can be observed during the synthesis of solid solutions from NW to NM. A shift in the ($\bar{1}$11) plane, characteristic of the NW phase, occurs due to the incorporation of Mo^{6+} cations into the lattice. These shifts are observed at smaller θ values, indicating the expansion of the crystal lattice. Among the analyzed samples, NW75 exhibited the greatest structural expansion, with a θ FWHM value of 0.48°. A 3D representation of the monoclinic structures of both NM and NW is illustrated in Fig. 1c.

The elemental analysis of W and Mo atoms, performed using XRF spectrometry, is presented in Table S1 of the ESI.† The results show that the compositions of both cations closely match the nominal values, confirming the formation of the NW75, NW50, and NW25 solid solutions.

To complement the experimental results, DFT calculations using the B3LYP and HSE06 functionals were performed to

This journal is © The Royal Society of Chemistry 2025

J. Mater. Chem. C, 2025, **13**, 6788–6798 | 6789

Table 1 Calculated values of the lattice parameters (a, b, and c in Å), β angle (°), and formation energy values (ΔE_f in Ry) for NW, NW75, NW50, NW25, and NM solid solutions, using the B3LYP and HSE06 functionals. For comparison, previously reported values are also included

Model	B3LYP					HSE06					Ref.
	A	b	c	β	ΔE_f	a	b	c	β	ΔE_f	
NW	4.578	5.759	4.803	87.66	−0.670	4.563	5.680	4.775	87.84	−0.678	[a]
NW75	4.585	5.734	4.822	88.01	−0.664	4.568	5.664	4.789	88.10	−0.672	[a]
NW50	4.590	5.714	4.840	88.26	−0.658	4.572	5.649	4.802	88.33	−0.665	[a]
NW25	4.595	5.692	4.859	88.64	−0.653	4.577	5.633	4.817	88.61	−0.659	[a]
NM	9.579	8.757	7.691	113.92	−0.647	9.512	8.682	7.659	114.13	−0.652	[a]
NW^exp	4.602	5.672	4.921	90.05	—						[7]
NW^exp	4.605	5.674	4.930	89.99	—						[36]
NW^theo	4.578	5.759	4.803	87.64	—						[7]
NM^exp	9.564	8.732	7.648	114.26	—						[38]
NM^theo	9.369	8.413	7.010	113.00	—						[39]

[a] This work.

determine the changes in lattice parameters and β angle associated with the substitution process of W^{6+} by Mo^{6+} cations. An analysis of the results in Table 1 shows good agreement between the theoretical results and the experimental data, as well as consistency with previous experimental and theoretical results reported in the literature. Furthermore, the results indicate that the formation of a solid solution leads to an increase in the a, b, and c lattice parameters and β values, resulting in lattice expansion from NW to NM. These findings are consistent with the shift in the (Ī11) peak observed earlier (see Fig. 1b).

The formation energy (ΔE_f) of the pure materials and the solid solutions was calculated, and the corresponding values are also presented in Table 1. Negative values of ΔE_f indicate greater stability of the crystal.[40] The pure NW with a more negative ΔE_f value exhibits greater stability compared to all solid solutions and pure NM.

In Fig. S1 and Table S2 of the ESI,† the calculated values of the Ni–O, W–O, and Mo–O bond distances, as well as the values of J–T distortion (σ_{JT}) for each $[NiO_6]$, $[WO_6]$ and $[MoO_6]$ cluster, which act as J–T active sites, are reported, obtained at the B3LYP level. Analysis of the results indicates that the geometric distortions of these clusters during the formation of solid solutions are minimal, i.e. low values of σ_{JT}. There are subtle changes in the local environment around the Ni^{2+}, W^{6+}, and Mo^{6+} cations. This result was anticipated, as the ionic radius (0.69 Å) and electronegativity (1.8) of the Mo^{6+} cation are similar to those of W^{6+} (0.66 Å and 1.7). An increase in the lattice parameter occurs only in NM due to the change in the point symmetry group, from $P2/c$ to $C2/m$.

In our case, the 3d orbitals of the Ni^{2+} cation in the octahedral environment of the $[NiO_6]$ cluster split into two degenerated sets of orbitals: t_{2g} orbitals (d_{xz}, d_{yz}, and d_{xy}) and e_g orbitals ($d_{x^2-y^2}$ and d_{z^2}). The adjacent $[WO_6]$ and $[MoO_6]$ clusters induce slight geometrical distortion (corresponding to elongated or compressed octahedra) to minimize the overall energy of the system, i.e. J–T distortion.

The Raman spectra of NW, NM, and solid solutions are presented in Fig. 2. According to group theory, 36 distinct Raman vibrational modes are present in these structures, of
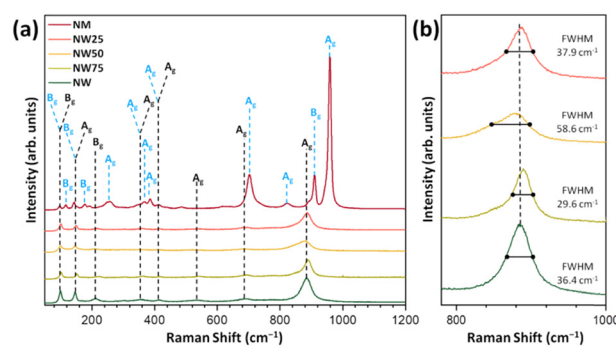

Fig. 2 (a) Raman spectra of the NW, NW75, NW50, NW25, and NM samples, with vertical lines indicating the positions and relative intensities of the experimental Raman-active modes. (b) Zoomed-in view of the band centered at 884 cm⁻¹.

which 18 are expected to be active modes ($8A_g + 10B_g$). As shown in Fig. 2a, the NW exhibits Raman modes at ≈100, 149, 416, 537, 695, and 885 cm⁻¹. The B_g vibrational mode at 100 cm⁻¹ with a low intensity is associated with the symmetric bending of O–Ni–O.[41]

The most intense mode at 884 cm⁻¹ (A_g mode) corresponds to the symmetric stretching of the W–O bond in the $[WO_6]$ cluster.[42] The Raman modes at 100, 140, 255, 368, 385, 704, 824, 911, and 960 cm⁻¹ are associated with NM. The weakly intense mode below 500 cm⁻¹ corresponds to the Raman-active Ni–O bond in the $[NiO_6]$ clusters.

Regarding the Mo–O bond in the $[MoO_6]$ clusters, the strongest band at 960 cm⁻¹ represents symmetric stretching, while the vibration signals at 824 cm⁻¹ and 811 cm⁻¹ correspond to asymmetric stretching.[20]

The FWHM values for the most intense Raman mode at 884 cm⁻¹, present in NW and NW75, NW50, and NW25 solid solutions, are 36.4, 29.6, 58.6, and 37.9 cm⁻¹, respectively (see Fig. 2b). Consequently, the NW50 sample exhibits a slight structural disorder in a short-range. The substitution of W^{6+} by Mo^{6+} may adjust the distortion of the local environment of the $[MoO_6]$ cluster and self-adapt the different structures of solid solutions. The relationship between this structural
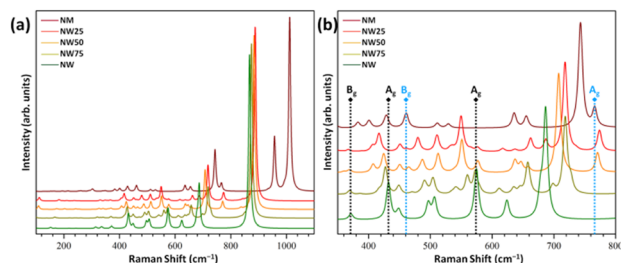
6790 | J. Mater. Chem. C, 2025, **13**, 6788–6798

This journal is © The Royal Society of Chemistry 2025

Fig. 3 (a) Theoretical Raman spectra of NW, NW75, NW50, NW25, and NM. (b) Zoomed-in view of the 350–800 cm^{-1} region. The black and blue vertical lines indicate the positions and relative intensities of the experimental Raman-active modes for NW and NM, respectively.

disorder, the composition of the conduction band (CB), and PL emissions will be discussed in the following sections.

The theoretical Raman spectra obtained at the B3LYP level are presented in Fig. 3a.

As observed experimentally (Fig. 2), the most intense peak in the NW structure, located at 867 cm^{-1} (A$_g$ mode), shifts with the increasing incorporation of Mo^{6+} cations. The Raman spectra in the 350–800 cm^{-1} range are highlighted in Fig. 3b. At 431 cm^{-1}, a shift to a lower wavelength is observed with increasing Mo^{6+} content, corresponding to the O–Ni–O bending (A$_g$ mode) in pure NW. Meanwhile, at 766 cm^{-1}, the A$_g$ mode associated with the Mo–O stretching in [MoO$_6$] clusters, characteristic of the NM structure, appears only in the NW50 and NW25 solid solutions. These results demonstrate an excellent correlation between the theoretical and experimental Raman spectra.

The infrared spectra are shown in Fig. 4. NW75, NW50, and NW25 solid solutions presented the same spectral profile as the pure NW sample. The A$_u$ mode located at around 877 cm^{-1}, corresponds to the symmetric stretching vibrations (O–W–O) in the distorted octahedral [WO$_6$] clusters, while the band at 837 cm^{-1} is associated with the optical B$_u$ mode. Another low-intensity band at 689 cm^{-1} can be attributed to the anti-symmetric stretching vibrations in the distorted octahedral
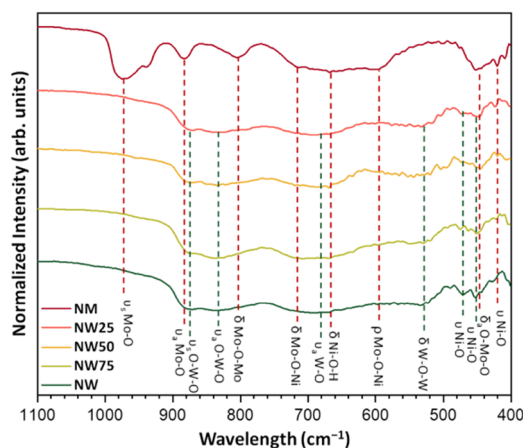
[WO$_6$] clusters. The band at 535 cm^{-1} corresponds to symmetric stretching vibrations (O–W–O–W–O) between [WO$_6$]–[WO$_6$] clusters. Additionally, the symmetric stretching vibrations (–O–Ni–O–) of the distorted octahedral [NiO$_6$] clusters were detected at 470 and 450 cm^{-1}.[43]

2.2 Morphological analysis

Fig. 5 shows the morphology and the average particle size distribution of all samples obtained from SEM images. As observed, the NW sample (Fig. 5a) exhibits faceted morphologies: however, with the increasing incorporation of Mo^{6+} cations, the particles became agglomerated and lost their defined morphology, as seen in Fig. 5(c, e, and g). The pure NW sample has an average size of 97.3 nm, while the NM sample has an average size of 39.4 nm.

For the NW75, NW50, and NW25 solid solutions, the average particle sizes were 39.4, 36.5, and 35.2 nm, respectively. Thus, the formation of the solid solution results in a reduction in particle size. This phenomenon may be attributed to short- and long-range structural changes that increase the system's disorder, ultimately leading to a decrease in particle size.

2.3 Electronic properties, DOS, and PL emissions

The diffuse reflectance spectroscopy graphs are shown in Fig. 6, where the NW and NM samples exhibit band gap energies (E_{gap}s) of 4.42 eV and 3.96 eV, respectively. The E_{gap} values of solid solutions decrease as the Mo^{6+} content increases (see Fig. 6 and Table 2). The theoretical calculations at the B3LYP and HSE06 levels reveal that the electronic transitions between the valence band (VB) and CB exhibit an indirect band gap, with the corresponding K-points in the Brillouin zone listed in Table 2. From NW to NW25, the indirect transition in the α
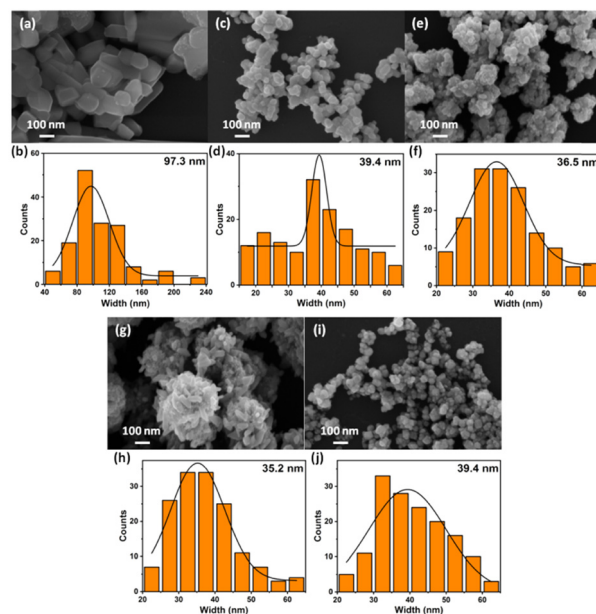

Fig. 5 SEM images and average particle size distribution for (a) and (b) NW, (c) and (d) NW75, (e) and (f) NW50, (g) and (h) NW25, and (i) and (j) NM samples.
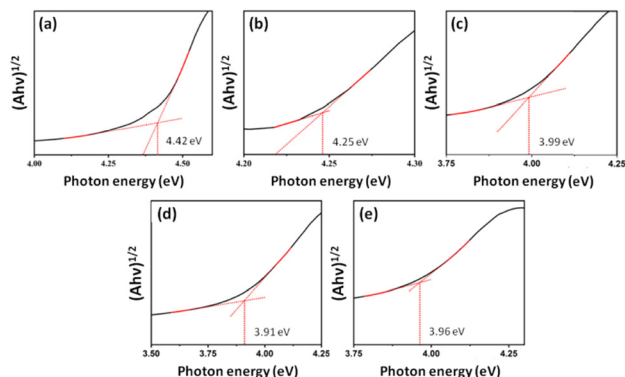

Fig. 4 Infrared spectra of NW, NW75, NW50, NW25, and NM samples. The vertical lines indicate the positions and assignation of the active modes.

This journal is © The Royal Society of Chemistry 2025

J. Mater. Chem. C, 2025, **13**, 6788–6798 | **6791**

Fig. 6 UV–vis spectra of (a) NW, (b) NW75, (c) NW50, (d) NW25, and (e) NM samples.

Fig. 7 (a) PL emissions and (b) CIE chromaticity diagram of the pure NW and NM, and NW75, NW50, and NW25 solid solutions.

channel, for both functionals, occurs between the Z-point in the VB and the Y-point in the CB, with the only difference being the K-point in the VB for NM. Additionally, in the β channel, the transition occurs between the Y-point in the VB and a different k-point in the CB, depending on the system. The experimental and calculated E_{gap} values for NW are higher than those for NM.

As the quantity of Mo^{6+} cations in the solid solution increases, the indirect E_{gap} values decrease, approaching the values observed for NM.

The formation of $NiW_{1-x}Mo_xO_4$ solid solutions introduces new energy states within the band gap region due to the presence of Mo^{6+} cations. Consequently, this leads to a shift in the Fermi energy levels and a reduction in the E_{gap}. The decrease in the optical E_{gap} value may be attributed to distortions in the $[WO_6]$, $[NiO_6]$, and $[MoO_6]$ clusters, which promote the creation of intermediary energy states between the VB and CB. These newly formed energy states are reflected in the DOS representation shown in Fig. 8.

The PL spectrum of the as-synthetized samples, shown in Fig. 7a, exhibits a broad emission range spanning from 400 to 650 nm, with an intense blue emission peak located at 450 nm observed for the NW50 sample. These broad emission bands in the visible region are commonly attributed to the recombination of trapped charge carriers,[44,45] which is associated with a distinctive multiphoton phenomenon. In this process, multiple
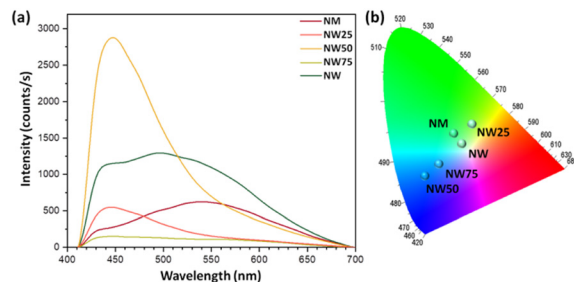
energy levels and/or different light emission centers can trap electrons within the band gap.

As electrons in these intermediate electronic states combine with holes from the VB, this process induces radiative recombination, leading to the appearance of PL emission lines.[46,47]

The PL emission data of pure NW and NM, as well as the NW75, NW50, and NW25 solid solutions, were used to construct the chromaticity diagram shown in Fig. 7b, to visualize the change in the color emission perceptible to the human eye. This analysis was performed using the coordinates of the Commission Internationale de l'Eclairage (CIE), calculated with Spectralux software.[48] The pure NW sample emits in the green region, with a shift toward the blue region as the substitution of W^{6+} cations by Mo^{6+} increases up to 50%. In the NW25 sample, the emission shifts to greenish yellow.

Due to the higher presence of MoO_6 in the NW25 sample, its characteristics are like those of the pure NM sample, which also emits in the green region. However, the NW25 sample exhibits more efficient energy transfer between $[MoO_6]$ and $[WO_6]$.[49–51]

It is well established that the PL spectra of NW are associated with the intrinsic emission of the wolframite structure[49,52] and the presence of structural defects (oxygen vacancies in the crystal structure).[53] The blue and green emissions may be attributed to the intrinsic $[WO_6]$ clusters, $i.e.$, the WO_6^{6-} complex, with double emission from one and the same center $(^3T_{1u}-^1A_{1g})$, while the yellow emission results from recombination of electron–hole pairs localized at oxygen anions, as reported in the $ZnWO_4$ and $CdWO_4$ crystals by Ovechkin $et\ al.$[54] and Lammers $et\ al.$[55]

Table 2 Experimental and theoretical E_{gap} values (eV), obtained using the B3LYP and HSE06 levels, for the NW, NW25, NW50, NW75, and NM systems

Model	Exp.	B3LYP Direct (Γ–Γ) Alpha	Beta	Indirect Alpha		Beta		HSE06 Direct (Γ–Γ) Alpha	Beta	Indirect Alpha		Beta	
NW	4.42	4.33	3.60	3.95	Z–Y	3.54	Y–B	4.03	3.47	3.62	Z–Y	3.43	Y–Γ
NW75	4.25	4.03	3.35	3.59		3.26		3.81	3.26	3.36		3.19	
NW50	3.99	3.81	3.17	3.33		3.04		3.64	3.09	3.16		2.98	Y–A
NW25	3.91	3.81	3.08	3.27		2.97	Y–Γ	3.63	3.03	3.10		2.91	Y–Γ
NM	3.96	4.29	4.48	4.24	Γ–Y	4.40		4.12	4.37	4.04	A–Y	4.25	Y–C
NW[a]	3.00[21]	NW[b]	3.91[7]										
NM[a]	2.23[38]												

[a] Experimental. [b] Theoretical.

Other authors point out the presence of strong electron–phonon coupling, which may account for the blue band, while the transitions of T_{2u}–T_{2g} and T_{1g}–T_{2g} in the WO_6^{6-} complex are responsible for the appearance of the green and yellow bands.[52,56] On the other hand, Harshan et al.[41] proposed that the emission peaks in the range of 470–494 nm are related to the intensive transition between the ground state $^3A_{2g}$ and the excited state $^3T_1$ of Ni^{2+} ($3d^8$) cations in the distorted octahedral $[NiO_6]$ cluster.

After detailed analysis of the reported results on the PL emissions of molybdates with monoclinic symmetry, we conclude that the corresponding structures present the local coordination of Mo^{6+} as four, i.e., a tetrahedral $[MoO_4]$ cluster, belonging to the β-phase, as discussed in molybdates such as $MgMoO_4$[57] and $CoMoO_4$.[58,59] In contrast, six oxygen anions surround one Mo^{6+} cation to render the $[MoO_6]$ cluster, as present in the NM crystal lattice, corresponding to the α-phase, which belongs to the $C2/m$ space group.

Based on the above considerations, we argue that the nature of the PL emissions of NW and NM, as well as of the solid solutions, remains unclear. A detailed interpretation of the electronic structures of the solid solutions is made more challenging by the presence of spectral signatures of electronic states associated with $[NiO_6]$, $[WO_6]$, and $[MoO_6]$ clusters in our measurements. The presence of these electronic states leads to electron–hole recombination through intermediate energy levels, resulting in light emission during the PL process. However, the theoretical description of these electronic states, particularly the excited states, is challenging, as it requires high accuracy, which is beyond the scope of the present study.

In our case, we propose that the slight lattice distortions associated with the J–T effect in the $3d^8$ electronic configuration of Ni^{2+} cations at the $[NiO_6]$ cluster, which is sensitive to the crystal field environment of the adjacent $[WO_6]$ and $[MoO_6]$ clusters, promote charge transfer among these clusters to modulate the PL emissions. Therefore, taking advantage of the fact that PL emissions are sensitive to the composition of DOS, specifically to the electronic states forming the CB, we conducted systematic atom-level analysis on the orbital overlap between Ni^{2+} at the $[NiO_6]$ cluster and the adjacent $[WO_6]$ and $[MoO_6]$ clusters.

This orbital hybridization can be considered a signature of the electronic cloud in the CB, which may serve as a guide to understanding and rationalizing the PL emissions throughout the solid solution.

Previously, Evarestov et al.[60] showed that in NW, the VB is formed by hybridized O 2p and Ni 3d orbitals, whereas the CB is formed by the empty W 5d orbitals with an admixture of the empty Ni 3d (e_g) states at the bottom of the CB. In our case, using the B3LYP functional, detailed analysis of the total DOS in Fig. 8 reveals that the VB is formed by the contributions of O and Ni atoms, while the CB is derived mainly from the lattice former (W and/or Mo atoms), with a smaller contribution from O and Ni atoms.

It is well known that the hybridization between different orbitals plays a crucial role in determining the electronic
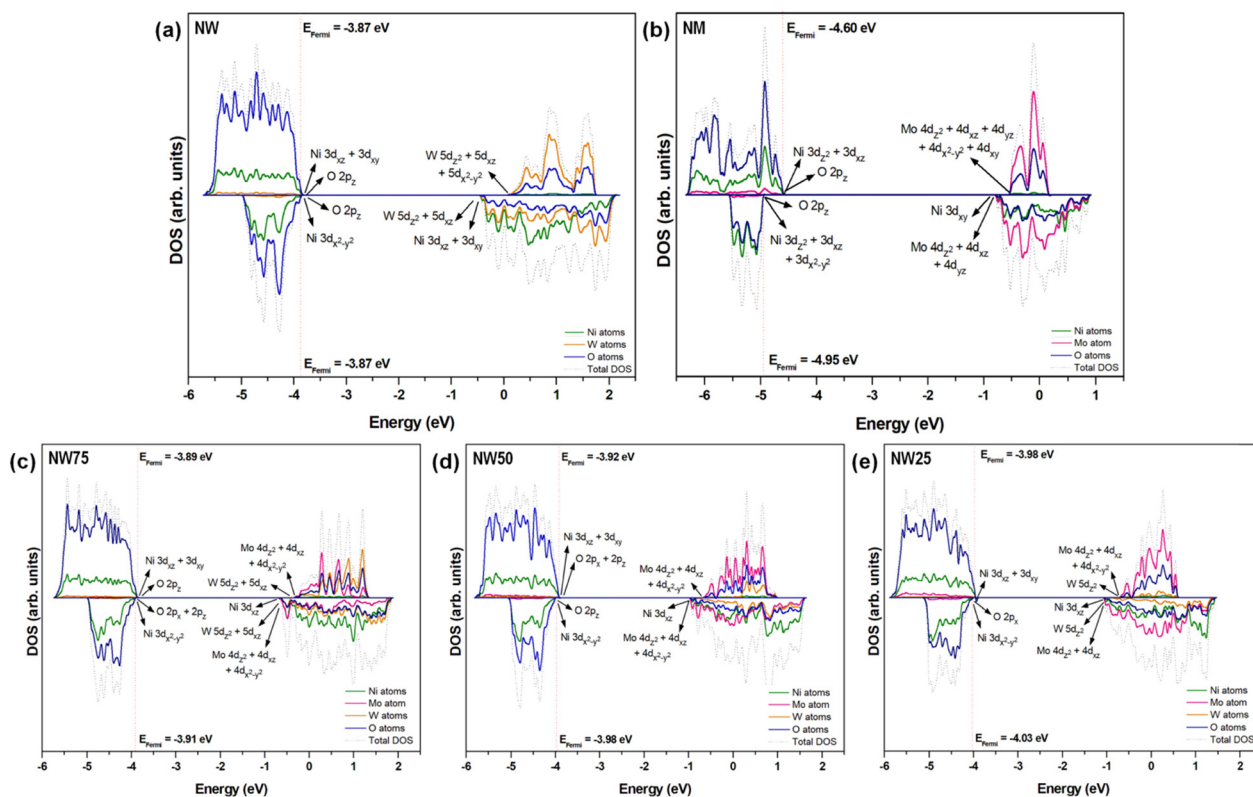

Fig. 8 Total DOS projected on Ni, W, Mo, and O atoms at the (a) pure NW and (b) NM and for the (c) NW75, (d) NW50, and (e) NW25 solid solutions.

This journal is © The Royal Society of Chemistry 2025

J. Mater. Chem. C, 2025, **13**, 6788–6798 | **6793**

properties of both NW and MN. Detailed analysis reveals that the top of the VB in the α channel at NW involves the hybridization of Ni $3d_{xz}$ + $3d_{xy}$ orbitals and O $2p_z$ orbitals, whereas the bottom of the CB is formed mainly by empty W $5d_{z^2}$ + $5d_{xz}$ + $5d_{x^2-y^2}$ orbitals. For the β channel, the VB is formed by Ni $3d_{x^2-y^2}$ orbitals hybridized with O $2p_z$ orbitals, while the CB is composed of the hybridization between W $5d_{z^2}$ + $5d_{xz}$ orbitals with Ni $3d_{xz}$ + $3d_{xy}$ orbitals. For NM, a similar profile is observed, with the top of the VB composed only of the Ni $3d_{xy}$ and $3d_{x^2-y^2}$ orbitals in the α and β channels, respectively. Regarding the bottom of the CB, the α channel is composed of empty Mo $4d_{z^2}$ + $4d_{xz}$ + $4d_{x^2-y^2}$ orbitals, while at the β channel, there is hybridization between the Mo $4d_{z^2}$ + $4d_{xz}$ orbitals with Ni $3d_{xz}$ orbitals. A more detailed analysis of the partial DOS for the NW (Fig. S2) and NM (Fig. S3) can be found in the ESI.†

During the formation of the NiW$_{1-x}$Mo$_x$O$_4$ solid solutions, small changes at the top of the VB are observed, particularly in the NW25 model, where hybridization between O $2p_x$ orbitals and Ni $3d_{x^2-y^2}$ orbitals occurs exclusively in the β channel. The Mo 4d orbitals become significant contributors to the bottom of the CB in both α and β channels. In NW75 and NW50, contributions from the W e_g orbitals and Mo $4d_{yz}$ orbital are observed. The atomic orbital contribution of W atoms in NW25 decreases and is represented by W $5d_{x^2-y^2}$ orbitals, maintaining the same Mo orbital contribution. Furthermore, as the NiW$_{1-x}$Mo$_x$O$_4$ solid solutions form, the Mo 4d orbital contribution to the CB increases at the bottom of this band in both α and β channels. In NW75, the Mo $4d_{z^2}$ + $4d_{xz}$ + $4d_{x^2-y^2}$ orbitals and W $5d_{z^2}$ + $5d_{xz}$ orbitals become the main components of the CB. On the other hand, in NW25, the W $5d_{z^2}$ orbital begins to contribute to the bottom of the CB.

An interesting observation is made for the NW50 solid solution: at the bottom of the CB, only the presence of Mo $4d_{z^2}$ + $4d_{xz}$ + $4d_{x^2-y^2}$ orbitals is detected, with no contribution from the W $5d_{z^2}$ orbitals. Therefore, for the solid solutions, the main changes are observed at the CB. The partial DOS projections onto orbitals can be found in the ESI† in Fig. S4–S6. Consequently, this leads to the emergence of spatially extensive hybrid bands at the CB, formed by subtle coupling among the Ni 3d, W 5d, Mo 4d, and O 2p orbitals. The corresponding charge-transfer configurations result from a complex mixing of orbitals, generating an electronic chain along the [NiO$_6$], [WO$_6$], and [MoO$_6$] clusters, thereby enhancing the transfer of photoexcited electrons to modulate the intensity of the PL emissions of the solid solutions. By exploiting previous analysis, our findings discern the assembled J–T effects at the [NiO$_6$], [WO$_6$], and [MoO$_6$] clusters to regulate the PL emissions and boost the orbital hybridization along the Ni–O–W/Mo framework of solid solutions (see Scheme 1).

To elucidate the electronic characteristic and the photogenerated charge migration mechanism within the solid solutions, the PL curves were analyzed in detail. The broad emission band was deconvoluted into three Gaussian curves, corresponding to emission peaks centered at 439, 483, and 557 nm (see Fig. 9).

As we know, samples with a higher contribution in the red or yellow regions, characterized by longer wavelengths, resulting
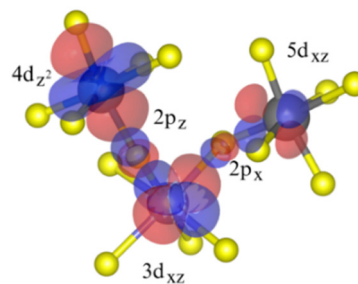
Scheme 1 Schematic illustration of the [NiO$_6$], [WO$_6$], and [MoO$_6$] clusters, as J–T active sites, which are assembled by orbital hybridization to drive the PL emissions.
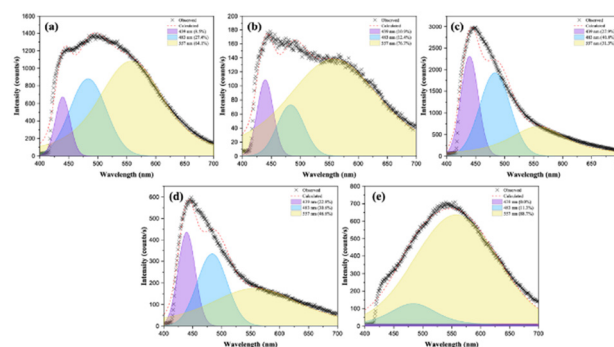
Fig. 9 PL deconvolution spectra of (a) NW, (b) NW75, (c) NW50, (d) NW25, and (e) NM samples.

from the presence of more defects in the lattice, such as deeper defects (e.g., oxygen vacancies). On the other hand, PL emission in the blue regions, at lower wavelengths, indicates the presence of more shallow defects, such as structural defects, with concomitant changes in the W/Mo–O distances and O–W/Mo–O angles. Indeed, slight structural defects, such as distortions in the local environment of Ni^{2+}, W^{6+}, and Mo^{6+}, can significantly affect the position and intensity of the observed PL emissions (see Fig. 7). Therefore, the NW25 sample exhibits deeper defects in the 557 nm region in the yellow (76.7%), similar to the pure NM sample (88.7%), while the NW50 sample shows more shallow defects at 483 nm in the blue region (40.8%). On the other hand, we can relate the peak at 439 nm to the orbital hybridization among the intra-cluster Ni–O–W/Mo framework at the CB, while the peaks at 483 and 557 nm correspond to the intrinsic emissions of [NiO$_6$] and [WO$_6$]/[MoO$_6$] clusters, respectively. As observed, the first and second parameters exhibit a maximum at NW50, while the contribution of the third is higher at pure NW and NM structures.

In this scenario, the modulation of PL emissions results from the hybridization of Mo $4d_{z^2}$ + $4d_{xz}$ + $4d_{x^2-y^2}$ orbitals into W $5d_{z^2}$ orbitals, thereby perturbing the electronic structure. This behavior plays a pivotal role in defining the electronic structure and the nature of PL emissions. Therefore, subtle changes occurring during the formation of the solid solution impact the E_{gap} values, the composition of the CB, and

6794 | *J. Mater. Chem. C*, 2025, **13**, 6788–6798

This journal is © The Royal Society of Chemistry 2025

cluster–cluster electronic transitions, ultimately modulating the PL emissions.

3 Conclusions

The synthesis of solid solutions is an effective strategy for fine-tuning the properties of advanced materials. This combined experimental and theoretical study enhances our understanding of the evolution of the structure, morphology, band gap, and PL from $NiWO_4$, homogeneous $NiW_{1-x}Mo_xO_4$ (x = 25, 50, and 75%) solid solutions to $NiMoO_4$. These materials were successfully synthesized via the co-precipitation method, followed by heat treatment in a conventional oven.

Their characterization was carried out using XRD, Raman, infrared, XRF, UV-vis, and PL spectroscopies, along with DFT calculations. The structural parameters and band gap values obtained using the B3LYP and HSE06 functionals show consistent results.

The main conclusions can be summarized as follows: (i) for $x \leq 50\%$, the substitution of W^{6+} by Mo^{6+} cations resulted in XRD patterns showing only peaks corresponding to the NW phase, while at x = 75%, characteristic peaks of the NM phase emerged alongside those of the NW phase; (ii) SEM images reveal agglomerated particles with no defined morphology, and a reduction in particle as the concentration of Mo^{6+} cations increases; (iii) DOS analysis indicates that the VB is primarily composed of Ni(3d) and O(2p) states, while the CB is mainly derived from W(5d)/Mo(4d) and O(2p) states; (iv) the formation of $NiW_{1-x}Mo_xO_4$ solid solutions introduces new energy states within the band gap region due to Mo^{6+} cations, leading to a shift in Fermi energy levels and a concomitant decrease in the E_{gap} value; (v) the significant enhancement of the PL emission intensity in the blue region at 483 nm of NW50 solid solution is attributed to shallow defects in the lattice and the contribution of 4d Mo orbitals to the CB; (vi) DFT calculations elucidate the role of competing emissions from $[NiO_6]$, $[WO_6]$ and $[MoO_6]$ clusters, establishing a relay mechanism based on an electron transport ladder through the Ni–O–W/Mo framework at the CB. This electronic channel is formed by J–T active sites ($[NiO_6]$, $[WO_6]$ and $[MoO_6]$ clusters), maximizing the orbital overlap of O(2p) with d orbitals from Ni, W, Mo cations, thereby driving the PL emission.

The conceptual framework constructed in this study provides a comprehensive understanding of the multifaceted characteristics of solid solutions. These findings highlight a novel approach for fine-tuning PL emissions by revealing the key hybridization of atomic orbitals within the complex DOS structure at the CB of semiconducting oxides. The diverse alignment patterns of J–T active sites ($[NiO_6]$, $[WO_6]$ and $[MoO_6]$ clusters) offer an in-depth insight into electronic coupling within a three-dimensional ordered structure.

Overall, this work advances our understanding of PL emission in solid solution by disentangling the subtle changes in the electronic structure of $[NiO_6]$, $[WO_6]$, and $[MoO_6]$ coordination environments, which is crucial for optical applications.

The proposed model can be extended to other solid solutions based on ternary metal oxides, providing a straightforward framework for rationalizing the relationship between the structure, electronic properties, and PL emissions, thereby guiding the design of solid solutions with tailored optical performance.

4 Experimental and theoretical methods

4.1 Synthesis

The samples were synthesized using the CP method, followed by heat treatment in a conventional oven. We began by synthesizing the pure NW and NM phases. For NW synthesis, 1×10^{-3} mol of $Na_2WO_4 \cdot 2H_2O$ (99.9%, Sigma-Aldrich) and 1×10^{-3} mol of $Ni(NO_3)_2 \cdot 6H_2O$ (99%, Sigma-Aldrich) were each diluted in two beakers with 50.0 mL of distilled water. The $Ni(NO_3)_2 \cdot 6H_2O$ solution was then added to the $Na_2WO_4 \cdot 2H_2O$ solution, forming a yellow precipitate. The final system was left under magnetic stirring at room temperature for 10 min. After this process, the precipitate was centrifuged, washed several times with distilled water ($\sim$pH 7), and dried in an oven at 60 °C for 12 h. The resulting powder was then placed in a conventional oven at 500 °C for 2 h, with a heating rate of 10 °C min^{-1}. The pure NM phase was synthesized in the same manner as NW, using Na_2MoO_4 (99.8% purity, Sigma-Aldrich) as the precursor. The same procedure was followed to prepare the $NiW_{1-x}Mo_xO_4$ (x = 25, 50, and 75%) solid solutions. Variations in the lattice former were implemented at concentrations of 25, 50, and 75% using Na_2MoO_4. The samples were labeled as NW75, NW50, and NW25 according to the percentage of W^{6+} cations remaining in the solid solution.

4.2 Characterization

The samples were characterized by XRD using a D/Max-2500PC diffractometer (Rigaku, Tokyo, Japan) with Cu Kα radiation (λ = 1.5406 Å) in the 2θ range of 10–80° and a scanning speed of 1° min^{-1}. XRF spectrometry was performed using an EDX-720 (Shimadzu). Raman spectra were recorded with an iHR550 spectrometer (Horiba Jobin-Yvon, Kyoto, Japan) coupled to a silicon charged-coupled-device (CCD) detector and an argon-ion laser (Melles Griot, Rochester, NY USA), operating at 514.5 nm with a maximum power of 200 mW. Fourier-transform infrared spectroscopy (Bruker Vector 22 FTIR, Billerica, MA USA) was used to record the samples' spectra in the 400–1100 cm^{-1} range. UV-vis diffuse-reflectance measurements were obtained using a Varian Cary spectrometer model 5G in the diffuse-reflectance mode, with a wavelength range of 200–800 nm and a scan speed of 600 nm min^{-1}. The morphologies of the samples were observed with a SEM operating at 5 kV (Supra 35-VP, Carl Zeiss, Jena, Germany). PL measurements were performed at room temperature by using a 355 nm laser (Cobolt/Zouk) as the excitation source, focused on a 200 μm spot at a constant power of 5 mW. The luminescence signal was dispersed using a 19.3 cm spectrometer (Andor/Kymera) and detected using a silicon CCD (Andor/IdusBU2).
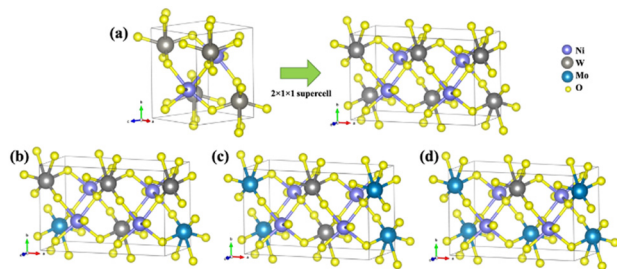
This journal is © The Royal Society of Chemistry 2025

J. Mater. Chem. C, 2025, **13**, 6788–6798 | **6795**

Fig. 10 (a) NW bulk model expanded in a $2 \times 1 \times 1$ supercell; (b) NW75 model; (c) NW50 model; and (d) NW25 model.

4.3 Computational methods and model systems

First-principles calculations for the models $NiW_{1-x}Mo_xO_4$ ($x =$ 25, 50, and 75%) solid solutions, as well as the pure NW and NM phases, were carried out using DFT with the B3LYP[61,62] hybrid functional, as implemented in the CRYSTAL17 program.[63] It is well known that the B3LYP functional tends to underestimate the band gap of solid-state materials.[64,65] To validate our computational approach, we performed additional calculations using the HSE06[66] functional, comparing the optimized structural parameters and band gap values with those obtained from B3LYP. The Ni, W, Mo, and O atoms were described using the 86-411(41d)G, Cora, SC_HAYWSC-311(d31)G, and 6-31d1 bases sets, respectively.[67] Regarding the diagonalization of the density matrix, the reciprocal space was sampled using a shrinking factor of 6, generated according to the Monkhorst–Pack scheme. The accuracy of the Coulomb and exchange series evaluation was controlled by five thresholds, set to 10^{-8}, 10^{-8}, 10^{-8}, 10^{-8}, and 10^{-16}.

For modelling solid solutions, the NW was represented by a $2 \times 1 \times 1$ supercell, resulting in a model with a 4-unit molecular formula in the structure ($Z = 4$). From this NW supercell, W^{6+} cations were substituted by Mo^{6+} cations according to the experimental data (25, 50, and 75%), as illustrated in Fig. 10. The NM bulk, which has a $C2/m$ structure, was modeled without expansion since its unit cell already contains a 4-unit molecular formula ($Z = 4$).

The formation energy (ΔE_f) of the NW75, NW50, and NW25 solid solutions was calculated using the following equation:[68–70]

$$\Delta E_f = \frac{E_f - (wE_{Ni} + xE_W + yE_O + zE_{Mo})}{(w + x + y + z)} \qquad (1)$$

where E_{Ni}, E_W, E_O, and E_{Mo} denote the total energy per atom of the pure Ni, W, O, and Mo elements, respectively, with w, x, y, and z representing the number of each atom in the cell model. The term $wE_{Ni} + xE_W + yE_O + zE_{Mo}$ corresponds to the sum of the energies of the constituent elements, while E_f is the total energy obtained from the optimization calculation. The Jahn–Teller (J–T) distortion parameter was employed to quantify the degree of distortion in the $[NiO_6]$, $[WO_6]$, and $[MoO_6]$ clusters and is defined as follows:

$$\sigma_{JT} = \sqrt{\frac{1}{6} \sum_{i=1}^{6} (r_i - \langle r_i \rangle)^2} \qquad (2)$$

where r_i represents the six metal–oxygen (Ni, W, and Mo–O) bond distances in the octahedral clusters, and r_i is the average bond distance.[71] The analysis of the structural and electronic properties was also performed using the CRYSTAL17 program.

The partial and total DOS of the models were generated along the appropriate high-symmetry directions of the corresponding irreducible Brillouin zone.

Author contributions

Data availability

The data will be made available upon request.

Conflicts of interest

The authors declare that they have no known competing financial interests or personal relationships that could have appeared to influence the work reported in this paper.

Acknowledgements

6796 | *J. Mater. Chem. C*, 2025, **13**, 6788–6798

This journal is © The Royal Society of Chemistry 2025

References

1 H. Arandiyan and M. Parvari, *Braz. J. Chem. Eng.*, 2009, **26**, 63–74.

2 J. Vieten, B. Bulfin, P. Huck, M. Horton, D. Guban, L. Zhu, Y. Lu, K. A. Persson, M. Roeb and C. Sattler, *Energy Environ. Sci.*, 2019, **12**, 1369–1384.

3 K. Maeda and K. Domen, *Chem. Mater.*, 2010, **22**, 612–623.

4 P. de Sousa, I. Nogueira, G. Gusmão, S. Gusmão, F. Lopes, B. Sousa, J. C. Sczancoski, A. Gouveia and L. S. Cavalcante, *J. Mater. Sci.: Mater. Electron.*, 2022, **33**, 22127–22152.

5 H. L. Abubakar, J. O. Tijani, S. A. Abdulkareem, A. Mann and S. Mustapha, *Heliyon*, 2022, **8**, e09964.

6 H. Azevedo, R. A. Raimundo, L. S. Ferreira, M. M. S. Silva, M. A. Morales, D. A. Macedo, U. U. Gomes and D. G. L. Cavalcante, *Mater. Chem. Phys.*, 2020, **242**, 122544.

7 F. J. O. Rosal, A. F. Gouveia, J. C. Sczancoski, P. S. Lemos, E. Longo, B. Zhang and L. S. Cavalcante, *Inorg. Chem. Commun.*, 2018, **48**, 34–40.

8 Y. L. Oliveira, A. F. Gouveia, M. J. S. Costa, F. H. P. Lopes, J. C. Sczancoski, E. Longo, G. E. Luz Jr., R. S. Santos and L. S. Cavalcante, *Mater. Sci. Energy Technol.*, 2022, **5**, 125–144.

9 R. A. P. Ribeiro, M. C. Oliveira, A. G. de Sousa, M. R. D. Bomio, F. V. Motta, L. Gracia, S. R. de Lazaro, E. Longo and J. Andres, *J. Appl. Phys.*, 2019, **126**, 235301.

10 S. Balasurya, M. K. Okla, I. A. Alaraidh, W. Soufan, A. A. Al-ghamdi, S. R. Ahamad, M. A. Abdel-Maksoud, H. AbdElgawad, L. L. Raju, A. M. Thomas and S. S. Khan, *Chemosphere*, 2022, **297**, 10.

11 A. M. Sorouri, A. Sobhani-Nasab, M. R. Ganjali, S. Manani, H. Ehrlich, Y. Joseph and M. Rahimi-Nasrabadi, *Appl. Mater. Today*, 2023, **32**, 101819.

12 A. Kumar, P. Sharma, G. Sharma, P. Dhiman, M. Shekh, M. Sillanpää and F. J. Stadler, *J. Alloys Compd.*, 2023, 172665.

13 A. Kuzmin, J. Purans, R. Kalendarev, D. Pailharey and Y. Mathey, *Electrochim. Acta*, 2001, **46**, 2233–2236.

14 D. Ma, H. Niu, J. Huang, Q. Li, J. Sun, H. Cai, Z. Zhou and J. Wang, *Nano Lett.*, 2024, **24**, 814–821.

15 R. Yang, X. F. Guo, K. Song, X. F. Bai, L. H. Jia, X. S. Chen, X. Wang and J. Wang, *Ceram. Int.*, 2021, **47**, 11349–11357.

16 A. E. Reddy, T. Anitha, C. Gopi, S. S. Rao and H. J. Kim, *Dalton Trans.*, 2018, **47**, 9057–9063.

17 T. Xiong, B. Huang, J. Wei, X. Yao, R. Xiao, Z. Zhu, F. Yang, Y. Huang, H. Yang and M.-S. J. T. Balogun, *J. Energy Chem.*, 2022, **67**, 805–813.

18 P. Sharma, M. Minakshi, J. Whale, A. Jean-Fulcrand and G. Garnweitner, *Nanomaterials*, 2021, **11**, 580.

19 N. A. Lima, L. D. S. Alencar, M. Siu-Li, C. A. C. Feitosa, A. Mesquita, J.-C. M'peko and M. I. B. Bernardi, *J. Adv. Ceram.*, 2020, **9**, 55–63.

20 A. Rajput, M. K. Adak and B. Chakraborty, *Inorg. Chem.*, 2022, **61**, 11189–11206.

21 D. Errandonea, F. Rodriguez, R. Vilaplana, D. Vie, S. Garg, B. Nayak, N. Garg, J. Singh, V. Kanchana and G. Vaitheeswaran, *J. Phys. Chem. C*, 2023, **127**, 15630–15640.

22 C. Liu, Z. He, Y. Liu, R. Chen, M. Shi, H. Zhu, C. Dong and J. Wang, *J. Magn. Magn. Mater.*, 2017, **444**, 190–192.

23 B. R. Ibiapina, A. E. Lima, L. K. Ribeiro, J. F. Cruz-Filho, A. G. Sales, M. A. Ramos, J. A. Sousa, D. Souza, Y. G. Gobato and F. E. Santos, *Environ. Sci. Pollut. Res.*, 2022, **29**, 79343–79356.

24 A. G. Sales, B. R. Ibiapina, G. S. Sales, J. F. Cruz-Filho, A. E. Lima, G. L. da Paz, R. R. Garcia, A. Correa, B. C. Viana and G. O. Gusmão, *J. Solid State Chem.*, 2023, **318**, 123773.

25 S. K. Ray and J. Hur, *J. Environ. Manage.*, 2021, **278**, 111562.

26 W. d S. Pereira, M. M. Ferrer, G. Botelho, L. Gracia, I. C. Nogueira, I. M. Pinatti, I. L. V. Rosa, F. d A. La Porta, J. Andrés and E. Longo, *Phys. Chem. Chem. Phys.*, 2016, **18**, 21966–21975.

27 P. F. S. Pereira, C. C. Santos, A. F. Gouveia, M. M. Ferrer, I. M. Pinatti, G. Botelho, J. R. Sambrano, I. L. V. Rosa, J. Andres and E. Longo, *Inorg. Chem.*, 2017, **56**, 7360–7372.

28 M. D. P. Silva, R. F. Goncalves, I. C. Nogueira, V. M. Longo, L. Mondoni, M. G. Moron, Y. V. Santana and E. Longo, *Spectrochim. Acta, Part A*, 2016, **153**, 428–435.

29 M. D. Penha, A. F. Gouveia, M. M. Teixeira, R. C. de Oliveira, M. Assis, J. R. Sambrano, F. Yokaichya, C. C. Santos, R. F. Gonçalves, M. Siu Li, M. A. San-Miguel, J. Andrés and E. Longo, *Mater. Res. Bull.*, 2020, **132**, 111011.

30 I. M. Pinatti, P. F. S. Pereira, M. de Assis, E. Longo and I. L. V. Rosa, *J. Alloys Compd.*, 2019, **771**, 433–447.

31 P. F. Pereira, C. C. De Foggi, A. F. Gouveia, I. M. Pinatti, L. A. Cabral, E. Guillamon, I. Sorribes, M. A. San-Miguel, C. E. Vergani, A. Z. Simões, E. Z. da Silva, L. S. Cavalcante, R. Llusar, E. Longo and J. Andrés, *Int. J. Mol. Sci.*, 2022, **23**, 10589.

32 M. C. Oliveira, J. Andres, L. Gracia, M. de Oliveira, J. M. R. Mercury, E. Longo and I. C. Nogueira, *Appl. Surf. Sci.*, 2019, **463**, 907–917.

33 E. O. Gomes, L. Gracia, A. A. G. Santiago, R. L. Tranquilin, F. V. Motta, R. A. C. Amoresi, E. Longo, M. R. D. Bomio and J. Andres, *Phys. Chem. Chem. Phys.*, 2020, **22**, 25876–25891.

34 A. F. Gouveia, R. A. Roca, N. G. Macedo, L. S. Cavalcante, E. Longo, M. A. San-Miguel, A. Altomare, G. S. da Silva and J. Andrés, *J. Mater. Res. Technol.*, 2022, **21**, 4023–4051.

35 R. C. Dickson, T. D. Manning, E. S. Raj, J. C. Booth, M. J. Rosseinsky and M. S. Dyer, *Phys. Chem. Chem. Phys.*, 2022, **24**, 16374–16387.

36 L. Araújo, M. Costa, B. Sousa, P. de Sousa, R. Monção, A. Araújo, R. de Sousa, F. Santos, R. Santos and L. Cavalcante, *J. Energy Storage*, 2024, **77**, 109999.

37 M. A. Ehsan and A. Khan, *ACS Omega*, 2021, **6**, 31339–31347.

38 L. Yang, J. Wang, Y. Wan, Y. Li, H. Xie, H. Cheng and H. J. Seo, *J. Alloys Compd.*, 2016, **664**, 756–763.

39 S. F. Matar, A. Largeteau and G. Demazeau, *Solid State Sci.*, 2010, **12**, 1779–1785.

40 N. A. Zarkevich, T. L. Tan and D. D. Johnson, *Phys. Rev. B: Condens. Matter Mater. Phys.*, 2007, **75**, 104203.

This journal is © The Royal Society of Chemistry 2025

J. Mater. Chem. C, 2025, **13**, 6788–6798 | **6797**

41 H. Harshan, K. P. Priyanka, A. Sreedevi, A. Jose and T. Varghese, *Eur. Phys. J. B*, 2018, **91**, 287.

42 B. Akila, S. Sakthinathan, T.-W. Chiu, J. N. Baby and M. George, *ACS Appl. Eng. Mater.*, 2024, **2**, 1663–1671.

43 Y. L. Oliveira, M. J. S. Costa, A. C. S. Juca, L. K. R. Silva, E. Longo, N. S. Arul and L. S. Cavalcante, *J. Mol. Struct.*, 2020, **1221**, 128774.

44 L. De Haart, A. De Vries and G. Blasse, *J. Solid State Chem.*, 1985, **59**, 291–300.

45 R. Leonelli and J. Brebner, *Phys. Rev. B: Condens. Matter Mater. Phys.*, 1986, **33**, 8649.

46 L. Gracia, J. Andres, V. Longo, J. A. Varela and E. Longo, *Chem. Phys. Lett.*, 2010, **493**, 141–146.

47 V. M. Longo, L. S. Cavalcante, M. G. Costa, M. L. Moreira, A. T. de Figueiredo, J. Andrés, J. A. Varela and E. Longo, *Theor. Chem. Acc.*, 2009, **124**, 385–394.

48 E. I. Stearns, *Commission Internationale de L'Éclairage, Colorimetry. Color Res. Appl., Publication CIE No. 15.2, 78*, Central Bureau of the CIE, Gaithersburg, MD, 2nd edn, 1987.

49 N. A. Lima, L. D. Alencar, M. Siu-Li, C. A. Feitosa, A. Mesquita, J.-C. M'peko and M. I. Bernardi, *J. Adv. Ceram.*, 2020, **9**, 55–63.

50 C. Macchi, G. M. Petinardi, L. A. Freire, M. S. Castro, C. M. Aldao, T. M. Luiz, F. Moura, A. Z. Simões, H. Moreno and E. Longo, *Dalton Trans.*, 2024, **53**, 525–534.

51 M. V. da Silva, D. F. M. de Oliveira, H. S. Oliveira and K. P. F. Siqueiras, *Mater. Res. Bull.*, 2020, **122**, 110665.

52 A. Mohammadi, Z. Amouzegar, M. Aminzare, M. Jafari and M. Nasr-Esfahani, *Mater. Res. Innovations*, 2017, **21**, 407–412.

53 M. Anicete-Santos, E. Orhan, M. De Maurera, L. Simoes, A. Souza, P. Pizani, E. Leite, J. A. Varela, J. Andrés and A. Beltrán, *Phys. Rev. B: Condens. Matter Mater. Phys.*, 2007, **75**, 165105.

54 A. Ovechkin, V. Ryzhikov, G. Tamulaitis and A. Žukauskas, *Phys. Status Solidi A*, 1987, **103**, 285–290.

55 M. Lammers, G. Blasse and D. Robertson, *Phys. Status Solidi A*, 1981, **63**, 569–572.

56 L. Grigorjeva, R. Deych, D. Millers and S. Chernov, *Radiat. Meas.*, 1998, **29**, 267–271.

57 A. A. Santiago, M. C. Oliveira, R. A. Ribeiro, R. L. Tranquilin, E. Longo, S. R. de Lazaro, F. V. Motta and M. R. Bomio, *Cryst. Growth Des.*, 2020, **20**, 6592–6603.

58 K. Seevakan, A. Manikandan, P. Devendran, A. Baykal and T. Alagesan, *Ceram. Int.*, 2018, **44**, 17735–17742.

59 R. Wangkhem, K. Khupfu, N. Yaiphaba and N. S. Singh, *Phys. Rev. B*, 2024, 416353.

60 A. Kuzmin, A. Kalinko and R. Evarestov, *Open Phys.*, 2011, **9**, 502–509.

61 A. D. Becke, *J. Chem. Phys.*, 1993, **98**, 5648–5652.

62 C. T. Lee, W. T. Yang and R. G. Parr, *Phys. Rev. B: Condens. Matter Mater. Phys.*, 1988, **37**, 785–789.

63 R. Dovesi, A. Erba, R. Orlando, C. M. Zicovich-Wilson, B. Civalleri, L. Maschio, M. Rérat, S. Casassa, J. Baima, S. Salustro and B. Kirtman, *Wiley Interdiscip. Rev.: Comput. Mol. Sci.*, 2018, **8**, e1360.

64 R. Shinde, S. S. R. K. C. Yamijala and B. M. Wong, *J. Phys.: Condens. Matter*, 2021, **33**, 115501.

65 B. G. Janesko, T. M. Henderson and G. E. Scuseria, *Phys. Chem. Chem. Phys.*, 2009, **11**, 443–454.

66 A. V. Krukau, O. A. Vydrov, A. F. Izmaylov and G. E. Scuseria, *J. Chem. Phys.*, 2006, **125**, 224106.

67 R. Dovesi, R. Orlando, B. Civalleri, C. Roetti, V. R. Saunders and C. M. Zicovich-Wilson, Crystal Basis Sets Library, 2025, https://www.crystal.unito.it/basis_sets.html.

68 D. P. Rai, A. Laref, A. Shankar, Sandeep, A. P. Sakhya, R. Khenata and R. K. Thapa, *J. Phys. Chem. Solids*, 2018, **120**, 104–108.

69 D. P. Rai, A. Shankar, Sandeep, M. P. Ghimire, R. Khenata and R. K. Thapa, *RSC Adv.*, 2015, **5**, 95353–95359.

70 A. B. Trench, T. R. Machado, A. F. Gouveia, M. Assis, L. G. da Trindade, C. Santos, A. Perrin, C. Perrin, M. Oliva, J. Andres and E. Longo, *Appl. Catal., B*, 2018, **238**, 198–211.

71 G. Bakradze, E. Welter and A. Kuzmin, *J. Phys. Chem. Solids*, 2023, **172**, 111052.

6798 | *J. Mater. Chem. C*, 2025, **13**, 6788–6798

This journal is © The Royal Society of Chemistry 2025